Long-lived magnetic field in earth-like terrestrial planets

D Andrault, Laure Pison, Julien Monteux, Emmanuel Gardés, A Mathieu

Physics of the Earth and Planetary Interiors 360 (2025) 107315

Contents lists available at ScienceDirect

Physics of the Earth and Planetary Interiors

journal homepage: www.elsevier.com/locate/pepi

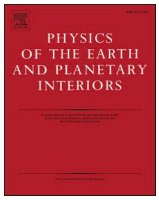

Long-lived magnetic field in earth-like terrestrial planets

D. Andrault *, L. Pison Pacynski, J. Monteux, E. Gardés, A. Mathieu

Université Clermont Auvergne, CNRS, IRD, OPGC, Laboratoire Magmas et Volcans, F-63000 Clermont-Ferrand, France

ARTICLE INFO

Keywords:
Experimental determination of the Fe thermal conductivity
Thermal evolution of the core
Generation of dynamo on Earth's like planets

ABSTRACT

We do not know precisely whether powering a planetary magnetic field is a common or rare feature of Earth-like planets, and for how many billion years it should likely be operating. If planetary dynamos should be driven by internal heat flow essentially (i.e. thermally driven dynamo, TDD), the answer relies on the energy budget of the planetary interior. On Earth, the Moon-forming impact provided a lot of energy ~4.5 billion years ago and the magnetic field remains strong until present. Despite extensive work on this subject, the controversial nature of the outer-core's thermal conductivity (k_{Cond}) makes the energy budget of the core open to discussions. Here we present new experimental constraints on the evolution of k_{Cond} with pressure from 22 to 150 GPa and temperature from 1050 to 2700 K. k_{Cond} is obtained by numerical modeling of the mechanism of propagation of a short heat pulse through a thin foil of iron loaded, compressed and heated in the laser-heated diamond anvil cell. With good coverage of large P-T domains, the accuracy of our measurements enables an accurate modeling of k_{Cond} as a function of the molar volume of Fe and temperature. We refine a value of 37(5) W/m/K at P-T conditions found at the Earth core-mantle boundary (CMB). If the geodynamo should be TDD essentially, this implies CMB cooling by 380–450 K over the entire Earth history and an inner core 1.9(4) billion years old. By comparing the mantle efficiency to extract heat at the CMB with the power requirement to sustain a TDD, we show that the geodynamo is unlikely to stop until the Earth's core is solidified. This effect comes from a decreasing power requirement to generate the dynamo with decreasing the temperature at the CMB. Now applying our P-T dependent k_{Cond} model to terrestrial planets with various external radii and fractions of silicate and metal, we show that the core size is a critical parameter. For a core smaller than a critical size, mantle convection induces a sufficient CMB heat flow to enable a TDD. This can explain absence of dynamo on Mars and possibly on Venus also if its core would be relatively large. Calculations show that exoplanets 1.5 times heavier than the Earth are unlikely to present an alive TDD, especially if they present large bulk densities. In contrast, the small exoplanets reported to date could host a TDD.

1. Introduction

1.1. Core thermal state along the Earth's history

Stochastic models of planetary accretion show high probability of late major impacts on growing Earth-like planets. During such catastrophic event, a tremendous amount of energy is provided to the deep planetary interior, which resets the primordial thermochemical structure (Nakajima and Stevenson, 2015). Much of this energy is mobilized before the solidification of the deep magma ocean. Various numerical models suggest a magma ocean lifetime of between a few thousand and a million years, depending on the efficiency of the atmosphere to blanket the planet surface (Lebrun et al., 2013; Monteux et al., 2016). In addition, the final temperature at the CMB is expected to be just above the solidus of the overlying mantle (Miller et al., 1991; Monteux et al., 2016). The reason for this is the free escape of heat from a hot core, through the magma ocean and towards the Earth surface, until a robust heat barrier made of solid material eventually decreases dramatically the cooling rate of the deep interior. This barrier can only be constituted of the liquidus phase, bridgmanite, which solidification starts when the profiles of magma ocean temperature and mantle liquidus cross in the deep mantle. Production of a sufficiently large amount of bridgmanite and accumulation of it at a given depth require the magma ocean temperature to be between the mantle solidus and liquidus profiles in a large range of depths in the deep lower mantle (Andrault, 2019; Miller et al., 1991; Stixrude et al., 2009). This is only possible when the CMB temperature is a few 100 K above the solidus of the overlying mantle.

Today, the thermal state of the deep Earth is constrained by coupling

* Corresponding author.
E-mail address: denis.andrault@uca.fr (D. Andrault).

https://doi.org/10.1016/j.pepi.2025.107315
Received 26 July 2024; Received in revised form 18 January 2025; Accepted 20 January 2025
Available online 25 January 2025

geophysical observations and mineral physics experiments. A mostly solid lowermost mantle with regional partially molten ultra-low velocity zones suggests a CMB temperature several 100 K below the dry-mantle solidus (McNamara et al., 2010). In parallel, presence of a solid inner core of ~1220 km radius is associated to solidification/melting of the core Fe-alloy at the temperature of the inner core boundary (ICB). Accurate melting experiments performed on pure Fe up to 200 GPa extrapolate to melting at 6230 K at 330 GPa of the ICB (Anzellini et al., 2013). Correcting for a melting temperature depression of ~730 K to account for to the presence of light elements (Morard et al., 2014), it yields an ICB temperature of ~5500 K. The CMB and ICB anchors of temperature define a steep temperature profile in the outer core that corresponds well to an adiabatic temperature gradient (∇T_{Adiab}). A slightly super adiabatic profile would favor thermally driven convection or, alternatively, a slightly sub adiabatic profile would help maintaining chemical stratification in the outer core (Buffett, 2014). However, the very low viscosity of the liquid Fe-alloy is likely to induce minimum divergence of the temperature profile from ∇T_{Adiab}.

Throughout Earth's history, major contributions to the core energy budget have been core cooling, radiogenic heating, latent heat of inner core crystallization and gravitational energy released by the migration of light elements. Each of these components has contributed with varying importance to induce movements in the outer-core and therefore to the generation of the geodynamo. We note, however, that the heat flux at the CMB ($\varnothing_{LM}$) is controlled by mantle properties. The dynamics of the mantle is mostly independent of the core energy budget, with the noticeable exception of a common temperature at the CMB. We thus expect a relatively smooth evolution of $\varnothing_{LM}$ over the geological ages, with some possible variations when, in particular, the planetary surface evolved from stagnant-lid to modern plate tectonics around the Archean to Proterozoic transition. Nevertheless, paleo evidences of a steady magnetic field on Earth for the last >3.5 billion years (Tarduno et al., 2015) require $\varnothing_{LM}$ to be large at all ages, whatever the amplitude of variation of the core energy budget over time.

1.2. Heat flux along the core adiabatic temperature gradient

A major parameter controlling the energy budget of the core of terrestrial planets and, as a consequence, of the powering of a thermally driven dynamo (TDD), is the thermal conductivity of the Fe-alloy of the outer cores (k_{Cond}). Three different methods have been used to constrain k_{Cond}: direct experimental measurements of k_{Cond}, indirect experimental measurements of electrical resistivity (ρ_{Elec}) from which thermal conductivity (k_{Elec}) can be derived based on the Wiedemann–Franz relation $k = LT/\rho$ (see Eq. 2 in Method section below), and ab initio calculations (k_{Abinit}). For CMB pressure and temperature (P-T) conditions, several works report k_{Elec} of about 100 W/m/K or more, due to ρ_{Elec} of 1μΩm or lower (see reviews in (Berrada and Secco, 2021; Williams, 2018)). This is compatible with reports of k_{Abinit} ~ 125 W/m/K (de Koker et al., 2012; Pozzo et al., 2012). It suggests present-day $\varnothing_{LM}$ of ~11 TW and core cooling (ΔT) by ~1500 K over the Earth history, when considering the presence of 100 ppm of radiogenic potassium in the outer core (Davies et al., 2015; Labrosse, 2015). Such large ΔT requires either a CMB temperature that remains much higher than the mantle liquidus for 1–2 billion of years, or a very low CMB temperature today, which are both difficult to reconcile with other available constraints.

Direct measurements of thermal conductivity are very scarce due to experimental difficulties. This technique has proved highly effective in determining the k_{Cond} of metals, including Pt, up to very high P-T conditions (McWilliams et al., 2015). By studying the time of propagation of a pulse of heat through a Fe foil, k_{Cond} was reported to be 33(7) W/m/K for pure Fe (Konôpková et al., 2016) and ~20 W/m/K for a Fe—Si alloy with 15 % Si (Hsieh et al., 2020) at CMB P-T conditions. Another work reported 61(9) and 157(73) W/m/K along the a and c axis of the hcp lattice of ε-Fe, respectively, for experiments performed at 300 K (Ohta et al., 2018). Finally, k_{Cond} was tentatively refined from the numerical modeling of thermal gradients in the diamond anvil cell (DAC) during continuous laser heating. It yielded k_{Cond} between ~30 to ~80 W/m/K at pressures of 45 to 70 GPa and moderate temperatures (Bulatov et al., 2020; Konôpková et al., 2011; Saha et al., 2020).

The present-day divergence by a factor of two or more between indirect-electrical and direct-thermal conductivity measurements can arise from either experimental issues or deviation of the Wiedemann–Franz relation. Electron–electron scattering could contribute to decreasing k_{Cond} at high temperatures. Still, the amplitude of this effect was reported to be insufficient to solve the current controversy (Pourovskii et al., 2020).

1.3. Strategy of our new experimental measurements

We developed a new strategy to probe the propagation of a heat pulse through a thin foil of Fe loaded in the laser-heated DAC. Compared to (Konôpková et al., 2016), the major originality relies on the use of high-sensitivity high-speed photodetectors to detect temperature changes due to heat pulse propagation (i) at a nominal temperature as low as 1000 K, (ii) with amplitude of less than 100 K, and (iii) on both sides of the hot sample simultaneously. The photodiodes record the thermal emission at the sample surface in a broad range of wavelengths around 800 nm. The time lag between the maximum temperatures on both sides of the sample is detectable immediately (Fig. 1b). As thickness of the Fe-foil is a major controlling parameter, it was measured before and after the experiments and monitored in situ at high P-T (Fig. 1a). To achieve a robust quantitative determination of k_{Cond}, we coupled our experiments to numerical strategies to reproduce adequately the thermal signals emitted from both sides of the sample.

2. Experimental methods

2.1. Generating P-T conditions

Pressure up to 150 GPa was generated in a membrane-driven diamond anvil cell (DAC) with beveled anvils presenting culets inner diameter of 250, 150, 100 or 70 μm. We used pre-indented rhenium gaskets with holes between 30 and 100 μm diameter. The use of hole diameter of ~1/3 that of the diamond culet prevents large sample deformation upon compression and decompression. Starting material consisted in small spheres of pure Fe (Good fellow, 99 % purity) with diameter of 10–40 μm, which were transformed into disks of ~2 to ~7 μm thickness. For experiments, Fe-foils were loaded between two dry KCl pellets, which were also pre-pressed between two diamonds. All steps of the sample loadings were performed inside a glove bag with a flux of dry air to prevent adsorption of water. Sample compression to nominal pressures between 20 and 150 GPa was monitored based on the shift of ruby fluorescence peaks and/or main Raman band of the diamond. Both measurements agree within 3 %. We used large Fe-foils covering ~75 % of the surface of the experimental chamber to make the two sample sides perfectly independent from each other from an optical point of view. Indeed, light pollution from one side to the other simply disables determination of k_{Cond} using the heat pulse method. We recorded optical images of the experimental chambers at many steps of the compression and decompression, in order to follow in situ deformation of the Fe-foil (Suppl. Fig. 1; Suppl. Table 1).

Double-side laser heating was performed using two continuous fiber lasers (1 μm wavelength) (Suppl. Fig. 2). With an initial laser diameter of ~5 mm, the laser spot was ~10 μm diameter (FWHM) on the sample. We used achromatic Schwarzschild lenses to capture thermal radiation from the center of the hot spot. Optical paths for incoming lasers and outgoing thermal emission signals were remotely adjusted using piezoelectric actuators. The nominal sample temperature (T_{Nom}) is determined at a time scale of a second with an optical spectrometer. We performed T_{Nom} between ~1050 K and ~ 2700 K, with an uncertainty of ~30 K and a temperature difference smaller than 20 K between the two sample sides.

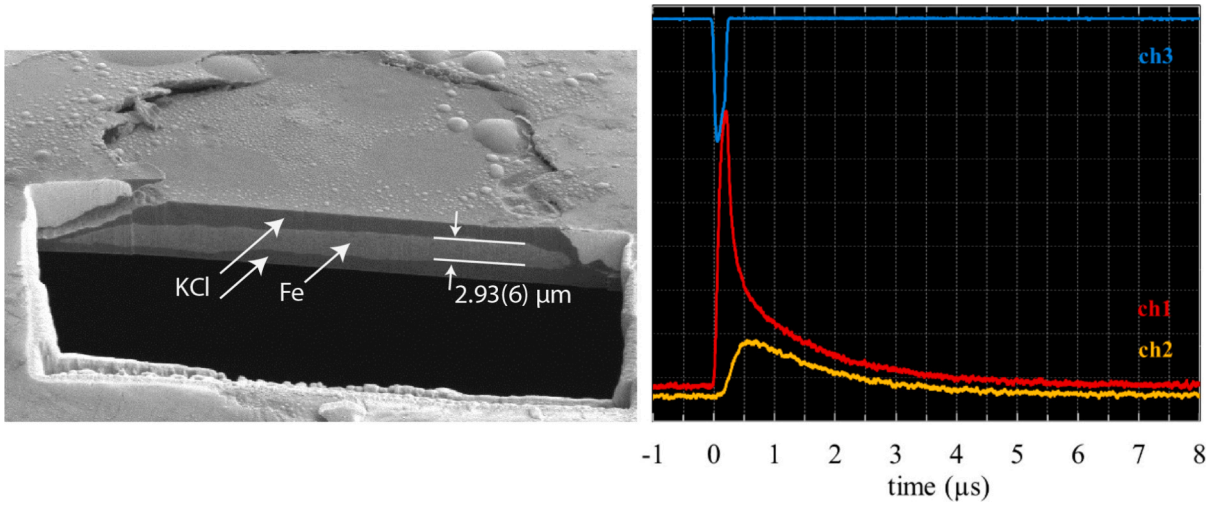

Fig. 1. Primary measurements: (**A, left**) Scanning electron image of an ion-milled cross-section of the sample recovered after compression in the diamond anvil cell to a nominal pressure of 100 GPa and steady laser-heating to 2136 K. The Fe-foil is embedded between two KCl thin plates. (**B, right**) Blue, red and yellow profiles are the photodetector responses to pulsed-laser radiation of ~200 ns duration, Fe-foil temperature on the pulse-laser side, Fe-foil temperature on the opposite side, respectively. Vertical axis is output voltage of photodiodes (arbitrary units). (For interpretation of the references to colour in this figure legend, the reader is referred to the web version of this article.)

This level of precision is achieved after the careful calibration of the optical response of our optical system and the sample emissivity, against a calibrated tungsten lamp (see (Pierru et al., 2022) and references therein). All our experimental temperatures remained lower than the melting point of Fe, as we gave priority to the quality of the k_{Cond} determination. Indeed, the geometry and thickness of the Fe-foil can vary upon melting, which would yield erroneous k_{Cond} determination in the liquid state. Thus, we had to perform extrapolations from our measurements to the 3500–4000 K found at the CMB (see below). A pressure correction of 30 % of the theoretical thermal pressure is applied to account for heating the Fe-foil in a confined environment. More details on the experimental set-up can be found in (Pierru et al., 2022).

2.2. Propagation time of the heat pulse through the sample

A third pulsed fiber-laser was combined with one of the two continuous lasers and focused at the same sample position. Its positioning was optimized using another set of piezoelectric actuators. The pulse duration is ~0.2 µsec (Suppl. Fig. 3). In this work, we probed the sample response to the laser pulse on its both sides simultaneously and with a high time resolution (Fig. 1). To achieve this, part of the thermal emission was focused on a high-sensitivity avalanche photodetector (Hamamatsu Photonics) on both sides of the sample. A third photodetector was used to trigger the measurements with an oscilloscope, based on the time of emission of the laser pulse. Time resolution of the oscilloscope was set to 2 ns. With a laser-pulse repeated every 20 µsec, we could record raw spectra by summing 10^4 acquisitions in a few seconds. To avoid light pollution from one side of the sample to the other, we added a pinhole filter system between the sample hot spot and the photodetectors.

The photodiodes we used are sensitive to photons in the range of visible light. The output voltage (V_t) is quantitatively correlated with the number of photons emitted at the Fe-foil surfaces. V_t provides a reliable inform on the variation of the sample temperature during the propagation of the heat pulse using the Stefan-Boltzmann law ($T_{Surf} \propto V_t^{1/4}$). This approximation meets our experimental conditions because the temperature change induced by the laser pulses is less than 100 K and, therefore, the shape of the thermal emission spectrum is not significantly affected by the heat pulse (see details in Suppl. Fig. 4). Therefore, our strategy has been to determine T_{Nom} using the optical spectrometer and follow the changes of temperature (ΔT_{pulse} from T_{Nom} to T_t) generated by the pulse laser using the time-resolved photodiodes: $T_t = T_{Nom}(V_t/V_{Nom})^{1/4}$. As a result, uncertainties on T_{Nom} did not affect the accuracy of the k_{Cond} determination, which is globally 5 %.

Measurements were performed at several nominal pressures and at increasing temperatures (Table 1). Special care was given to minimize the intensity of the laser pulse not to induce a too important change of the sample temperature during the pulse propagation; but still to obtain a satisfactorily good signal on both sample sides. Temperature changes were typically smaller than 100 K.

2.3. FIB-SEM analyses of the recovered samples

All samples have been recovered to ambient P-T and the layered structure was revealed by ion thinning (Fig. 1b). Sample cutting and observations were performed using a dual microscope equipped with Xe plasma focused ion beam and high-resolution scanning electron microscope (FEG-SEM-FIB HELIOS microscope; Thermofisher). The rate of sample thinning allowed probing the entire sample volume. All samples revealed the Fe-foil embedded between two KCl plates. Noticeable variation of the sample and KCl thicknesses can be found at the positions where the Fe-foil was molten at the highest experimental temperatures. Apart from these regions, thicknesses are homogeneous. Reported thicknesses average values and expanded 2σ uncertainties result from 20 to 100 measurements on 4 to 5 different sample sections (Table 1).

2.4. Refinement of Fe-foils thickness at high pressure

Knowledge of the Fe-foil thickness (hp) is essential to the experimental determination of thermal conductivity k_{Cond} using the heat pulse method. Dependency between the two was empirically reported to be $k_{Cond} \propto hp^{1.5}$ (Lobanov and Geballe, 2022). In this work, we determine the sample thickness before compression and monitor the surface of the Fe-foil and of the pressure chamber during compression and decompression by optical observations, and finally determine the thickness of the recovered sample by FIB-SEM analyses (Suppl. Fig. 1; Table 1). Different effects can modify the thickness of the Fe-foil on the course of the experiment:

(i) Compression and thermal expansion of the Fe lattice. The amplitude of these effects at given experimental P-T conditions can be calculated based on the Fe equation of state (EoS, see below). The deformation can be isotropic or solely anisotropic if the Fe-foil would

Table 1
Experimental conditions.

Exp.	Culet	Nominal P	Gasket thickness (μm)			Fe-foil thickness (μm)					KCl thickness (μm)	
Number	Diameter (μm)	Po (GPa)	ho	hpo	hp	ho	hp-$_{OPT}$	hpo	Δhi	hp-$_{SEM}$	Laser side	Opposite side
Fe_07	250	22.0 ± 0.8	34	24.0	22.7	3.3 ± 0.3	3.0	3.04 ± 0.06	0.17	**2.87**	9.0	11
Fe_05	250	22.2 ± 0.8	36	24.4	23.0	7.5 ± 0.5	7.0	7.11 ± 0.08	0.39	**6.72**	8.2	8.2
Fe_03*	250	45.0 ± 1.6	36	–	16.2	6.0 ± 0.3	**4.7**	–	–	**–**	5.7	5.7
Fe_13	150	50.0 ± 1.8	30	12.4	11.1	5.7 ± 0.6	4.0	4.58 ± 0.20	0.37	**4.21**	3.4	3.4
Fe_03*	250	60.0 ± 2.1	–	14.4	12.7	–	–	3.78 ± 0.14	0.33	**3.44**	4.6	4.6
Fe_10	150	73.0 ± 2.6	21	8.59	7.40	5.4 ± 0.5	–	2.64 ± 0.08	0.25	**2.39**	2.3	2.7
Fe_04	150	77.0 ± 2.7	30	7.69	6.59	5.5 ± 0.4	2.0	2.44 ± 0.11	0.24	**2.20**	2.2	2.2
Fe_09	100	100 ± 3.5	21	5.69	4.72	4.4 ± 0.5	3.1	2.93 ± 0.06	0.33	**2.60**	0.7	1.4
Fe_06	106	106 ± 3.5	20	5.60	4.61	4.3 ± 0.4	2.6	1.84 ± 0.12	0.21	**1.63**	1.4	1.4
Fe_12	70	135 ± 4.7	12	4.04	3.22	3.0 ± 0.5	2.0	2.04 ± 0.07	0.26	**1.79**	1.0	0.4
Fe_08	70	139 ± 4.9	13	3.23	2.56	3.9 ± 0.5	2.1	2.48 ± 0.19	0.31	**2.16**	0.2	0.2
Fe_11	70	145 ± 5.1	14	3.75	2.96	5.3 ± 0.7	2.3	2.51 ± 0.07	0.32	**2.19**	0.2	0.7

* Thermal conductivity of sample Fe_03 was measured at two different experimental pressures. **For *Re*-gaskets**: *ho* is measured using micrometer before compression, *hpo* using SEM observations after decompression and *hp* is derived from *hpo* assuming preferential anisotropic decompression along the diamond axis of the *Re*-gasket. **For Fe-foils**: *ho* is initial thickness calculated from optical determinations of surface of the Fe-foil and diameter of the Fe-sphere used to produce the foil by crushing. *hp-$_{OPT}$* is derived from *ho* following the change of Fe-foil surface upon compression and applying a correction factor for static compression of the Fe-lattice. *hpo* is an average of 20 to 100 measurements (associated to standard deviations) on the recovered and ion-polished Fe-foil, using SEM. *Δhi* is the change of Fe-foil thickness expected for isotropic decompression of Fe and *hp-$_{SEM}$* is the estimated Fe-foil thickness during the experiments, based on SEM measurements (arguments for this are detailed in Suppl. Fig. 1). Numbers in bold were used to refine Fe thermal conductivity in our experiments. **For KCl insulating plates**: Thickness of KCl layers located on both sample sides (side on which is focused the pulsed laser, and opposite side) was refined by SEM measurements to determine the relative thicknesses between them and from the difference between the thicknesses of the gasket and of the Fe-foil at high pressures.

only shrink or expand along the axis of the two diamonds. Anisotropic behavior yields larger changes of *hp* with P-T than isotropic. The EoS shows much less significant effect of temperature than pressure, especially when heating induces some thermal pressure instead of Fe-lattice expansion. Here we consider that the Fe-foil thickness remains the same within experimental uncertainties upon heating.

(ii) Plastic deformation of the Fe-foil. It can be important when the experimental chamber also deforms upon compression and/or decompression, if the pressure medium does not accommodate the deformation. In a previous work, large opening of the gasket-hole was reported on decompression, with an amplitude of 70 % to 170 % of the gasket-hole surface depending on the nature of the pressure medium and maximum pressure (see Figs. S1 and S2 of (Lobanov and Geballe, 2022)). This effect can be associated to cupping of the diamond culet at high loads. Cupping induces larger diamond-diamond distance at the center of the culet, compared to the edges. Upon decompression, back flattening of the cupped culet (referred as "un-cupping" hereafter) can crush the sample located at the center, reduce its thickness and increase its surface, compared to that prevailing at the maximum pressure.

In our experiments, Fe-foils and experimental chambers do not show large deformation upon compression and decompression, whatever the diameter of diamond culets and the experimental pressure. This is nicely showed by several optical and SEM images recorded before, during and after the HP-HT experiments (see details in Suppl. Fig. 1). A likely reason for minor un-cupping in our experiments is the use of diamond culets deliberately smaller than those needed to achieve our experimental pressures. We used culets of 250/300, 150/300, 100/300 and 70/300 μm diameter to generate pressures of 20–50, 55–80, 100 et 135–150 GPa, compared to culets of 300, 150/300 et 100/300 μm used in previous work for pressures of 60, 85 et 110–150 GPa (Lobanov and Geballe, 2022), respectively. Less load on diamond inevitably yields less cupping at the experimental pressure and less un-cupping upon decompression (Hemley et al., 1997). This can explain why our samples encountered minor changes of their thickness (and surface) upon decompression. In addition, SEM observations of the recovered samples show that the KCl pressure medium could preferentially accommodate the deformation by expanding away from the compression chamber when decompression is complete (Suppl. Fig. 1).

We determine the thickness of the Fe-foil during the HP-HT experiments based on our determination of *hpo* the Fe-foils thickness determined using FIB-SEM on recovered samples. To account for the change of *hp* during decompression, we apply a correction corresponding to isotropic decompression of the Fe-foils. This is validated based on the detection of a small increase of the surfaces of samples and experimental chambers upon decompression (Table 1). Isotropic decompression is the behavior expected in presence of a relatively soft pressure medium, such as KCl. The calculated Fe-foil thicknesses are in very good agreement with those reported in very similar P-T conditions (Konôpková et al., 2016).

2.5. Finite element modeling of the temperature evolution

Accurate determination of k_{Cond} requires coupling our experimental measurements with numerical modeling of the time-dependent temperature field and heat transfer within the sample assembly. We used the simulation software COMSOL Multiphysics based on a finite element analysis. This commercial software was previously validated for two phase flow applications in several geodynamical contexts (e.g. (Qaddah et al., 2020)).

We modeled the heat transfer occurring in an extremely thin iron sample so we could reasonably neglect the advective heat transfer process. Hence, we used a numerical approach similar to (Konôpková et al., 2016) and we considered that the heat transfer occurs only via conduction:

$$\rho C_p \frac{\partial T}{\partial t} = k_{Cond} \nabla^2 T \quad (1)$$

where ρ, C_p, and k_{Cond} are the densities, heat capacities and thermal conductivities of the materials considered. We implemented an axisymmetric 2D geometry to reproduce the multilayer configuration of a Fe-foil sandwiched between two insulating layers of KCl, with a rhenium gasket at the edge, themselves trapped between the diamond anvils (Fig. 2a). In our models, we imposed the thermal conductivities listed in Suppl. Table 1 except the sample conductivity that we recovered by fitting the experimental signal. The temperature imposed at the boundary of our models is the room temperature with $T_{room} = 300$ K.

Eq. 1 was solved using the Heat Transfer tool-suite of COMSOL Multiphysics 5.4. Several benchmarks are available on their website (e.g. https://www.comsol.com/model/axisymmetric-transient-heat-transfer-267; See also the Code Availability section). The experimental

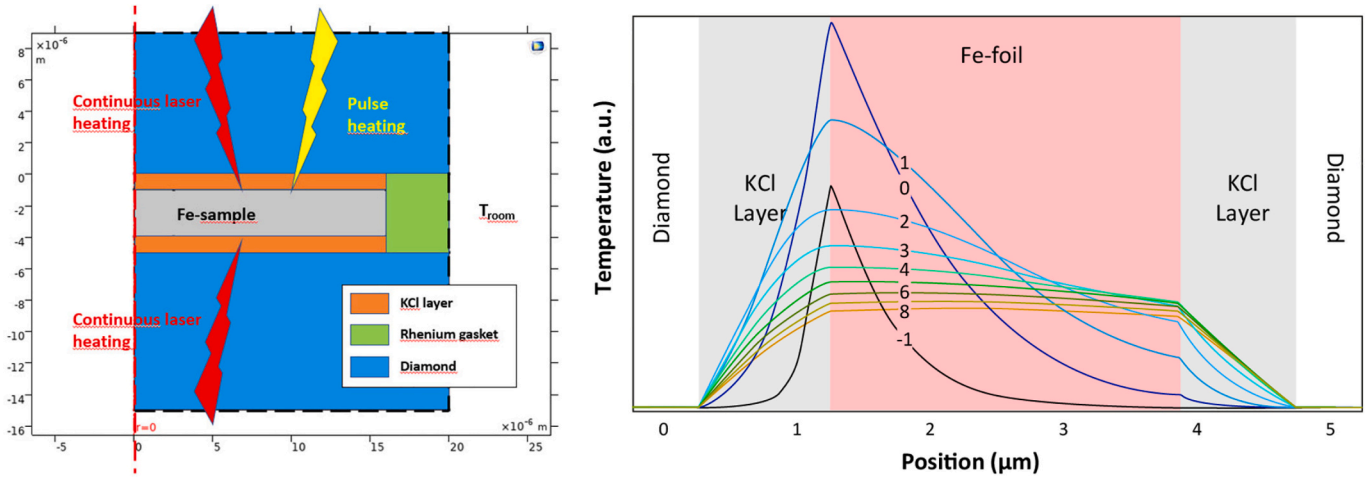

Fig. 2. (A, right) Sample configuration in numerical modeling. Finite element modeling is performed to analyze the propagation of heat in the Fe-foil, KCl insulator, rhenium gasket and diamond anvils. Major parameters are listed in Suppl. Table 1. **(B, left) Change with time of the temperature gradient across the Fe-foil**. The number attached to each curve reports the time relative to the maximum temperature at the sample surface (itself labelled "0"), in 10^{-7} s.

domain is modeled considering a 2D axisymmetric geometry (Fig. 2a). The software applies a finite-element method to a grid mesh. We tested the sensitivity of the mesh size on our results performing calculations for different sizes of the mesh (dx) between dx = 4dx$_{ref}$ (coarsest resolution) and dx = dx$_{ref}$/2 (finest resolution). Our tests show that convergence is already reached for dx$_{ref}$ = 1.8 × 10^{-7}m (Suppl. Fig. 5), which corresponds to nearly 16,000 elements in our computational domain.

Thicknesses of the different layers were adjusted to each experiment (Table 1). First, we modeled the temperature field generated by the two continuous fiber-lasers. We considered the laser energy deposited on the first 100 nm of the Fe-foil (Metzner et al., 2020). The lasers intensity was numerically adjusted until temperature at the sample surfaces reproduced the measured T_{Nom} of a given experiment. Then, we performed time-resolved calculations after adding a pulse of heat on one of the sample surfaces (Fig. 2b).

The experimental signal is affected by several experimental parameters (Farah et al., 2022). Fortunately, many of them affect the amplitude of ΔT_{pulse} but not its time-dependent profile. This arises because our measurements were performed based on very reduced heat perturbation, thanks to the use of the ultra-sensible photodiodes. As a result, several sample parameters can be considered constant during the travel of the heat pulse. It is the case of laser energy deposited at the sample surface, diamond temperature (T_{Diam}), thermal conductivities of KCl (K_{KCl}) and diamond (fixed to 2 and 9900 W/m/K, respectively; Suppl. Table 1) and also thicknesses of the KCl layers (Table 1) as long as they are not much thinner than the hot spot diameter. This is why we adjust the experimental signal by the theoretical one on the basis of the normalized photodiode signals.

Parameters having a major impact on signals are on the one hand the Fe-foil thickness, which mainly impacts the rate of temperature rise and the arrival time of the peak of maximum temperature, and on the other hand T_{Diam}, K_{KCl}, and the diameter of the hot spot on the sample (D_P), which impact mainly the rate of decay of ΔT with time. The refinement show that the three last parameters present a clear tradeoff between them and, therefore, we fixed T_{Diam} and K_{KCl} to reasonable values of 300 K and 2 W/m/K, respectively (see Suppl. Text and Suppl. Fig. 6). D_P was adjusted to 1 to 15 μm, decreasing with increasing P or T, to reproduce the photodiode signal recorded on the sample side where the pulse laser is focused. Then, the value of k_{Cond} was refined to reproduce at best the photodiode signal on the sample side opposite to the pulse-laser. Comparisons between our finite element modeling and the experimental results are illustrated in Suppl. Fig. 7A-D.

2.6. Formalism for P-T dependence of thermal conductivity

As thermal conductivity in metals is a process dominated by electron properties, electrical resistivity (ρ_{Elec}) and its derivatives make the relevant theoretical basis for discussing the evolution of k_{Cond} with P-T. The Wiedemann–Franz law establishes the relation between ρ_{Elec} and k_{Cond}.

$$k_{Cond} = LT/\rho_{Elec} \quad (2)$$

The value of L may diverge from the ideal value of $L_0 = 2.44\ 10^{-8}$ $W\Omega K^{-2}$ at the extreme P-T conditions found in our experiments and in planetary outer cores (Pourovskii et al., 2020; Secco, 2017). In particular, the continuous electron flow from hot to cold regions of the metal could induce an electrical field that slowdowns the electron flow in the temperature gradient. This is the well-known Seebeck effect (with parameter *Se*; see (Secco, 2017)):

$$L = L_0 - Se^2 \quad (3)$$

Nevertheless, electron conduction in Fe depends primarily on Fe—Fe interatomic distance and electron-phonon interactions. On one hand, the well-constrained PVT equation of state of Fe defines its volume variation (V/V_0, where V_0 is the reference Fe volume), which yields the Fe—Fe distance. In this work, we use a high temperature third-order Birch-Murnaghan equation of state with elastic parameters from (Garai et al., 2011) to determine the volume of both γ and ε forms of Fe. On the other hand, amplitude of the electron-phonon interactions can be modeled based on the ratio T/Θ_D, where Θ_D is the Debye temperature. We write:

$$\rho_{Elec}(V,T) = \rho_0\left(\frac{V}{V_0}\right)^a + \rho_1\left(\frac{T}{\Theta_D(V)}\right)^b \quad (4)$$

where ρ_0, ρ_1, a and b are constants and $\Theta_D(V)$ is the volume-dependent Debye temperature. The Bloch–Grüneisen formula suggests ρ_{Elec} proportional to T at high temperatures ($T > \Theta_D$), which is verified in our experiments (see Fig. 3 below). $\Theta_D(V)$ can be expressed as a function of the Fe Grüneisen parameter (γ):

$$\gamma = \frac{dln(\Theta_D)}{dln(V)}\Big)_T \quad (5)$$

Combining Eqs. (4) and (5) yields:

$$\rho_{Elec}(V,T) = \rho_0\left(\frac{V}{V_0}\right)^a + \rho_1\left(\left(\frac{V}{V_0}\right)^\gamma \frac{T}{\Theta_{D0}}\right)^b \quad (6)$$

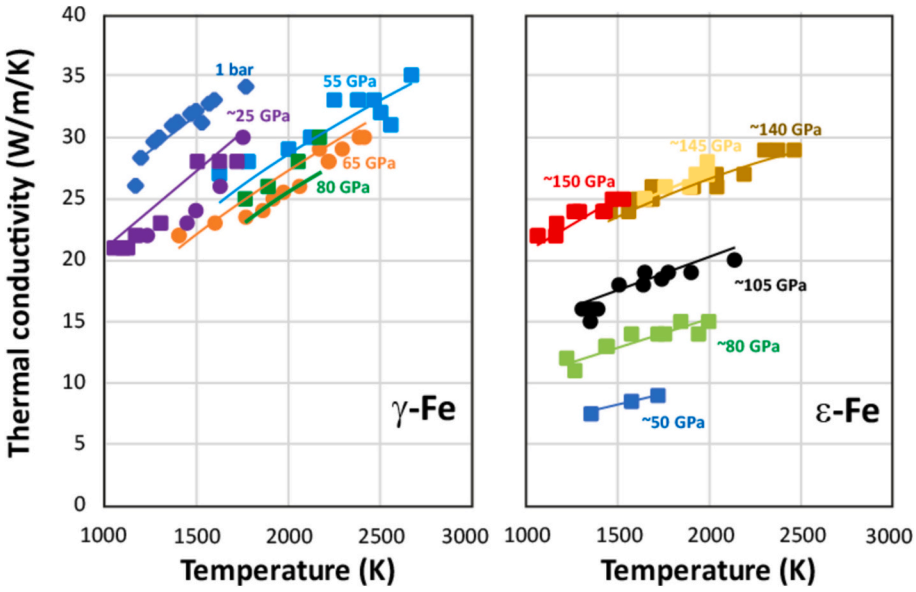

Fig. 3. Thermal conductivity results: (**A, left**) Colored symbols are thermal conductivities (k_{Cond}) measured in the P-T stability field of γ-Fe from ~25 to ~80 GPa and up to ~2500 K (Suppl. Table 2). Data available at 1 bar are also reported (see (Secco, 2017)). k_{Cond} increases with increasing temperature and decreases slightly with increasing pressure. (**B, right**) Measurements performed in the stability field of ε-Fe from ~50 to ~150 GPa and up to ~2700 K. k_{Cond} increases with increasing the nominal pressure and with increasing temperature. Thermal conductivity increases with temperature but decreases slightly with increasing pressure. In both diagrams, experimental data are labelled with an average experimental pressure and the true P-T conditions are reported in Suppl. Table 2. Light colored lines are fits to experimental data based on ε-k_{Cond} and γ-k_{Cond} models using Eqs. 2 and 6 and parameters reported in Table 2.

This expression is nearly identical to that used in previous work (de Koker et al., 2012), except for the exponent of temperature *b*. The value of this parameter is actually major as it defines the temperature dependence of thermal conductivity, through the Eq. 2. In this work, we fixed $\gamma = 1.3$ and $\Theta_{D0} = 470$ K (Anderson, 1998).

Previous works dedicated to the experimental determination of k_{Elec} (e.g. (Gomi et al., 2013; Yong et al., 2019)) report a linear variation of ρ_{Elec} with temperature (thus b ~ 1), suggesting a small variation of k_{Cond} with temperature (according to Eq. 2). Conversely, ab initio calculations (de Koker et al., 2012; Pozzo et al., 2012) or direct k_{Cond} measurements (Konôpková et al., 2016) report positive (corresponding to $b < 1$) and negative (corresponding to $b > 1$) correlations between k_{Cond} and *T*, respectively. Previous experimental study proposed $k_{Cond} \propto 1/\sqrt{T}$ (Konôpková et al., 2016) corresponding to $\rho_0 = 0$ and $b = 1.5$ in Eq. 6.

Finally, it has been proposed that the resistivity of Fe could be saturating at high temperature (Gomi et al., 2013; Pozzo et al., 2022). At the origin of this effect is the electron mean free path, which decreases significantly with increasing temperature, and which cannot be shorter than the interatomic distance between two adjacent Fe atoms. Above a critical temperature, the Fe resistivity should be insensitive to temperature, and the temperature limit could be 2500–3000 K (see (Pozzo et al., 2022) and references therein). In contrast, ρ_{Elec} should still depend on the Fe—Fe interatomic spacing, and thus on the P-T conditions. To take into account resistivity saturation, we calculate ρ_{Elec} (Eq. 6) considering the variation with P and T of the molar volume of Fe in the first term, and a second term constant above the saturation temperature.

3. Experimental results

We refined k_{Cond} values between 7.5 W/m/K and 35 W/m/K for pure Fe at pressures from 24 to 150 GPa and temperatures from 1050 K to 2700 K (Fig. 3, Suppl. Table 2). This P-T domain covers the stability field of two different forms of Fe; γ-fcc is found at high temperatures up to ~100 GPa and ε-hcp is the lower temperature form up to ~100 GPa and the only form at higher pressures (Anzellini et al., 2013). The results are different for experiments carried out in each stability field.

3.1. Experimental results for ε-Fe

For ε-Fe, there is a major increase with pressure of k_{Cond} from around 7 to 25 W/m/K, and a significant increase of k_{Cond} with temperature at all pressures. The entire data set is nicely fitted using Eq. 6, which models the change of ρ_{Elec} with volume and temperature. It defines an ε-k_{Cond} model (Table 2). If a ε-hcp lattice would prevail at the CMB conditions of 135 GPa and 3850 K, we should expect k_{Cond} of 31(3) W/m/K for pure-Fe, based on ε-k_{Cond} model.

Interestingly, the observed increase of k_{Cond} with increasing pressure that we observe is well compatible with previous ρ_{Elec} measurements performed at similar pressures and 300 K (Gomi et al., 2013) (Suppl. Fig. 8). An increase of k_{Cond} with temperature implies a moderate increase of ρ_{Elec} with temperature, based on the Wiedemann-Franz relation (Eq. 2). This is in qualitative agreement with previous reports of k_{Elec} and k_{Abinit} (de Koker et al., 2012; Gomi et al., 2013), but deviates from previous report of k_{Cond} found inversely proportional to $\sqrt{T}$ (Konôpková et al., 2016).

3.2. Experimental results for γ-Fe

The 1 bar value of k_{Cond} for γ-Fe was reported to increase from ~27 and ~ 34 W/m/K for temperatures between 1200 and 1600 K, respectively (see (Secco, 2017)). Our data show slight decrease of k_{cond} with increasing pressure at constant temperature (Fig. 3b), which yields to the γ-k_{Cond} model (Table 2). This effect is less pronounced but definitely opposite to that observed for ε-Fe. It is also opposite to the theoretical principle proposing a decrease of ρ_{Elec} when decreasing the Fe—Fe interatomic distance ($d_{Fe—Fe}$). However, several arguments mitigate that

Table 2
Electrical resistivity (ρ_{Elec}) model. Parameters *a*, *b*, ρ_0 and ρ_1 yield thermal conductivity (k_{Cond}) of pure Fe at given P-T conditions using Eqs. (2) and (6).

	ρ_0	a	ρ_1	b
ε-Fe	1.243E-05	9.00	3.779E-07	0.90
γ-Fe	6.393E-07	−3.60	1.803E-07	1.00

rule: (i) density of γ-Fe (and thus $d_{Fe—Fe}$) is roughly constant in the γ-Fe stability field extending from low-P/low-T to high-P/high-T (as can be modeled by γ-k_{Cond} model). (ii) Significant increase of ρ_{Elec} is also observed at the transition between body centered cubic to hexagonal compact forms of Fe upon compression at 300 K (Suppl. Fig. 8), despite decrease of $d_{Fe\text{-}Fe}$ by ~20 %. (iii) There may be changes in thermo-electric and/or electron-electron scattering effects that dominate the evolution with pressure (Pourovskii et al., 2020; Secco, 2017). Extrapolation to the CMB conditions of γ-k_{Cond} model yields 35(3) W/m/K for pure-Fe. This value is similar to that of ε-k_{Cond} model when accounting for uncertainties.

3.3. Comparison with previous reports of thermal and electrical conductivity

The k_{Cond} values of 31(3) and 35(3) W/m/K that we calculate for pure Fe at the Earth's CMB are well compatible with the 33(7) W/m/K obtained in a previous report based on comparable heat-pulse technique (Konôpková et al., 2016). However, this similarity at CMB conditions hides an opposite evolution of k_{Cond} with temperature; k_{Cond} decreases with temperature in this previous report, while it increases in ours (Fig. 4). It yields divergences when discussing the magnetic field of terrestrial planets presenting P-T conditions different from that of the Earth. While our temperature dependency agrees better with previous reports of k_{Elec} and k_{Abinit} (de Koker et al., 2012; Gomi et al., 2013), we still obtain k_{Cond} of pure-Fe at Earth's CMB ~3 times lower than the average value of ~100 W/m/K of these reports (Williams, 2018). Interestingly, previous reports of k_{Cond} and k_{Elec} of γ-Fe at 1 bar agree well with each other (Fig. 3a, (Secco, 2017) and references therein). Therefore, the discrepancy is built upon increasing P-T; Our γ-k_{Cond} is found nearly constant on the melting line (Fig. 5a), while k_{Elec} and k_{Abinit} increase.

A possible explanation for this effect is an increased divergence of the Lorentz number (L) from the ideal value $L_0 = 2.44\ 10^{-8}$ WΩK^{-2} on the melting line. A moderate decrease of L to ~$2.2\ 10^{-8}$ and $2.0\ 10^{-8}$ WΩK^{-2} at the P-T conditions of CMB and ICB, respectively, was proposed based on increasing electron–electron scattering in Fe (Pourovskii et al., 2020). While this correction goes in the right direction, its amplitude remains largely insufficient. A possible explanation is a major increase of the Seebeck coefficient of Fe with P-T (Eq. 3; (Berrada and Secco, 2021)). Such effect may also explain the different evolution with P-T of the γ-k_{Cond} and ε-k_{Cond} models (Fig. 3).

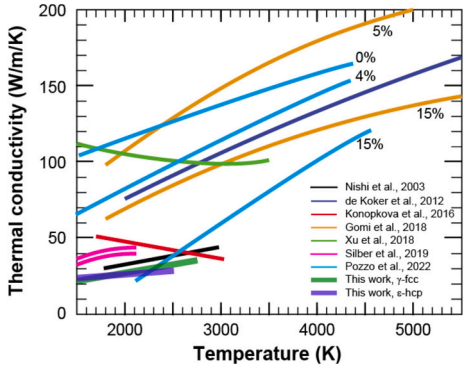

Fig. 4. Temperature dependence of conductivity; comparison with previous results: References are pure Fe at 1 bar (Nishi et al., 2003), 135 GPa (de Koker et al., 2012), Fe with 5 or 15 % C, N, or O at 120 GPa (Gomi and Yoshino, 2018), Fe at 140 GPa (Xu et al., 2018), Fe and FeSi at 9 GPa (Silber et al., 2019), Fe with 0, 4 and 15 % Si at 60–150 GPa (Pozzo et al., 2022). Results from this work is γ-fcc and ε-hcp for pressure ranges of 25–80 GPa and 140–150 GPa, respectively.

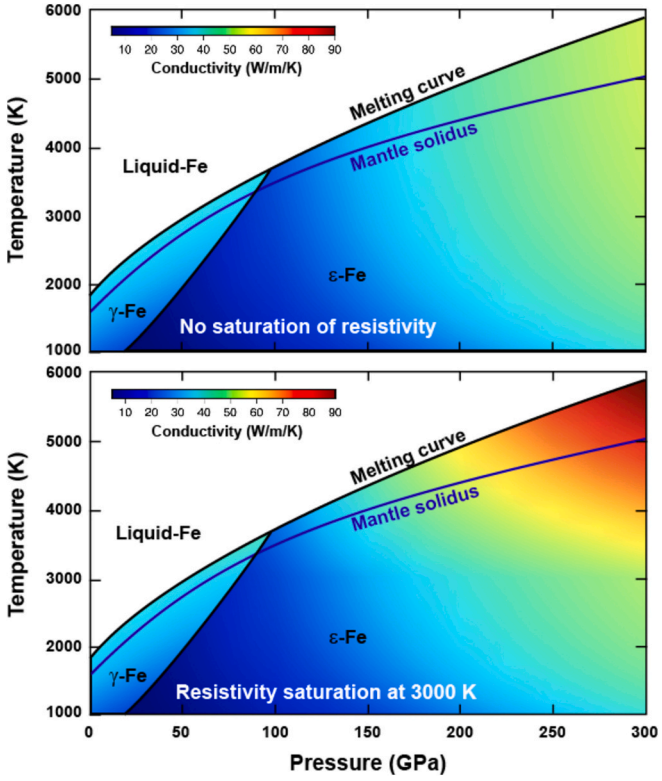

Fig. 5. Thermal conductivity of pure Fe at planetary P-T conditions. K_{Cond} is calculated at various P-T conditions using Eqs. (2) and (6) and the empirical parameters refined in this study (Table 2). (**Top**) and (**Bottom**) frames consider "no saturation" and "saturation at 3000 K", respectively, of electrical resistivity (see text). The colour code reports the value of K_{Cond} graphically in the P-T domains of stability of the γ or ε forms of Fe (Anzellini et al., 2013). Later in this work, we investigate the change with P-T of k_{Cond} along the mantle solidus or the melting curve of pure Fe (see Fig. 6a).

4. Discussions

We now investigate the impact of our experimental trends on the thermal state of the Earth along its history, as well as that of other terrestrial planets (i.e. exoplanets) that would also hold a geomagnetic field. For this, we first refine the dependence of k_{Cond} as a function of the volume of Fe and the outer core temperature, based on our experimental results (Fig. 3) and following Eqs. (2) and (6).

4.1. Thermal conductivity of Fe in planetary outer cores

Several assumptions are needed to address the thermal conductivity of planetary outer cores based on our experimental results:

- *We* consider three different possible temperature profiles for planetary CMBs located at varying pressures: (i) the melting curve of Fe (Anzellini et al., 2013), (ii) the solidus of a pyrolitic mantle (Pierru et al., 2022) and (iii) the solidus of pyrolite minus 300 K (as possibly arises for the Earth, today). It arises that the different temperature profiles have a moderate impact on the evolution of the k_{Cond} value with the CMB depth (Fig. 6a). We therefore consider CMB temperatures corresponding to the solidus of a pyrolitic-type mantle, in agreement with the modeling of the solidification of magma oceans (Monteux et al., 2016). We note that considering CMB temperatures several 100 K higher, or lower, does not affect much any of our conclusions.
- Between the evolutions of k_{Cond} for the γ and ε forms of Fe, adopting the γ-k_{Cond} model is well justified below ~100 GPa, when γ-Fe is the

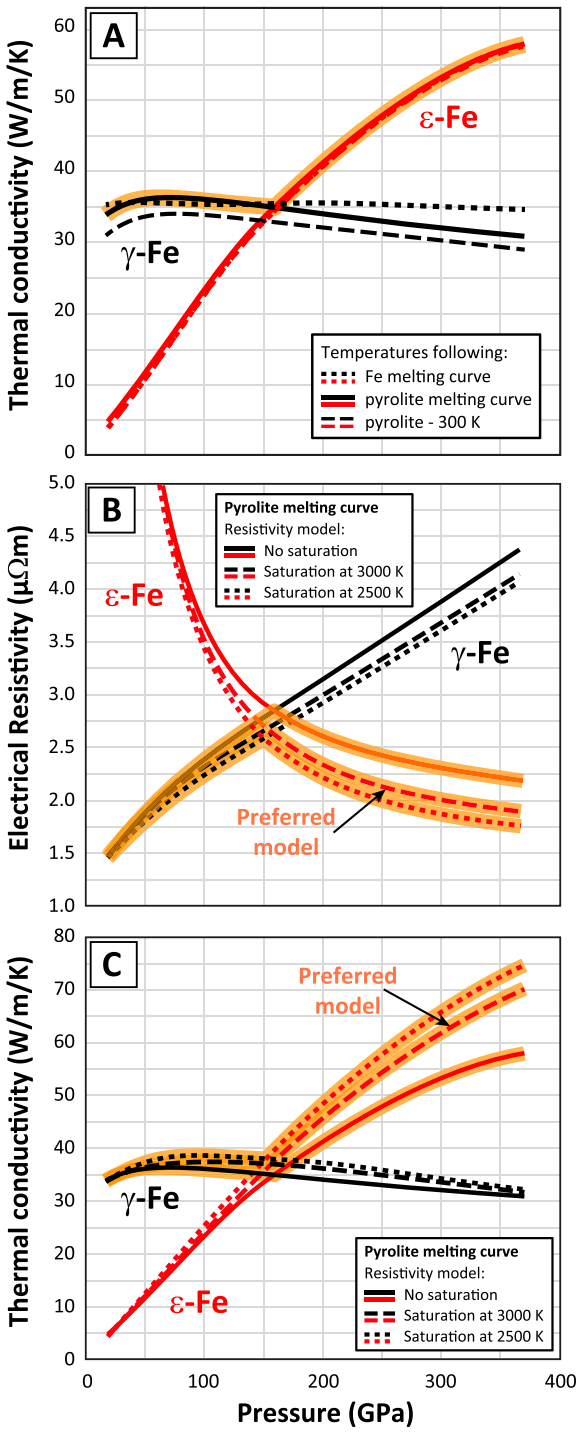

Fig. 6. Thermal conductivity of pure Fe: (A) Using γ and ε models of Fe (Table 2, Eqs. (2) and (6)), we calculate k_{Cond} at various core pressures, considering temperature evolutions typical of (i) the melting curve of Fe, (ii) the solidus of a pyrolitic mantle, and (iii) 300 K below the pyrolite solidus. According to the Fe phase diagram, γ and ε forms of Fe prevail in the solid state below and above a pressure of ~100 GPa, respectively (Anzellini et al., 2013). (B) We investigate the impact of the saturation of the Fe resistivity at temperatures of 3000 or 2500 K (see Methods). The P-T profile selected for planetary CMBs is the solidus of pyrolite. (C) Thermal conductivity at planetary CMB conditions for the same conditions as (b). When considering a k_{Cond} decrease by ~20 % to account for the presence of light elements in the outer cores, we calculate k_{Cond} values of 30(5) and 52(5) W/m/K at the Earth's CMB and ICB conditions, respectively.

solid phase below the melting curve. At pressures higher than ~100 GPa, ε-Fe should prevail (Anzellini et al., 2013). Our results suggest slightly lower k_{Cond} of ε-Fe, compared to γ-Fe, at pressures between 100 and ~160 GPa (Fig. 6a). However, with compression, the former increases, while the later decreases due to values of a parameters of opposite signs (Table 2). We calculate that ε-k_{Cond} and γ-k_{Cond} become equal at ~160 GPa. Still, our experimental precision is not sufficient to enforce a first order change in the value of k_{Cond} at the transition between γ and ε-Fe, especially in the liquid (see below). For this reason, we propose a smooth evolution of k_{Cond} with pressure, following the γ-k_{Cond} model up to ~160 GPa, where the two models intersect, and the ε-k_{Cond} model for pressures above (Fig. 6a). We acknowledge that the true evolution of k_{Cond} in outer cores could present a less sharp change of slope at ~160 GPa, because of progressive changes of the atomic local structure in the liquid state.

- *We* assume that k_{Cond} is not strongly affected by melting (i.e. equal above and below the melting temperature). This is a common assumption used in previous works, which has been validated by accurate experiments performed in large volume experiments at somewhat lower pressures (Manthilake et al., 2019; Secco, 2017). The assumption relies on an intense vibration of the atomic structure expected at temperatures far above the Debye temperature (For Fe, Θ_{D0} = 470 K). As a result, the electron mean free path is similar in the solid and the melt around the melting temperature. This assumption is further validated by the reports of a saturation of the Fe resistivity at temperatures above 2500–3000 K (Gomi et al., 2013; Pozzo et al., 2022); then, the controlling parameter for resistivity (and thus k_{Cond}, Eq. 2) is the Fe—Fe interatomic distance and not the state of Fe (Eq. 6).
- *We* consider that resistivity could be saturating at 3000 K, or even 2500 K, as suggested in previous works (Gomi et al., 2013; Pozzo et al., 2022). We find that the impact on ρ_{Elec} remains moderate at pressures lower than ~150 GPa (Figs. 5 and 6b). The divergence becomes more important for more extreme P-T conditions. It results an increase of k_{Cond} of 10–15 % at the Earth's CMB, which becomes 35–40 % at ICB conditions (Figs. 5 and 6c). For further calculations, we consider a saturation limit at 3000 K.
- Now accounting for the presence of light elements in planetary cores reduces k_{Cond} by 15 % to 30 % compared to pure Fe, as suggested by ab initio calculations (de Koker et al., 2012; Wagle et al., 2019). The reduction is due to the increase of the electron-phonon interactions in presence of impurities. We note that the amplitude of this effect could decrease with pressure (Silber et al., 2019) and may be less significant in the liquid state where the concepts of point defects and electron-phonon interactions become unclear. It was experimentally determined that 15 wt% Si could reduce k_{Cond} by a factor of two; however, it is unlikely that the Si-content in the outer core is that important (Hsieh et al., 2020). Here, we consider that the outer core k_{Cond} is decreased by 20 % due to the presence of light elements in the outer core.

It results a constant k_{Cond} of ~37(5) W/m/K on the Fe melting curve up to ~160 GPa (Fig. 6a). This characteristic was already proposed based on theoretical considerations (see (Stacey and Loper, 2007)). At pressures higher than 160 GPa, k_{Cond} increases up to ~65(4) W/m/K for P-T conditions of 330 GPa and ~ 5500 K, which correspond to the inner core boundary on Earth (Anzellini et al., 2013). Considering a 20 % decrease due to light elements, thermal conductivities of the Fe-alloy in the Earth's core becomes 30(5) and 52(5) W/m/K at CMB and ICB conditions, respectively.

4.2. *Energy budget of the core*

The core energy budget is usually written as:

$$\varnothing_{OC} = \varnothing_{Cooling} + \varnothing_{Rad} + \varnothing_{Cryst} + \varnothing_{Buoy} \quad (7)$$

where $\varnothing_{Oc}$, $\varnothing_{Cooling}$, $\varnothing_{Rad}$, $\varnothing_{Cryst}$ and $\varnothing_{Buoy}$ are heat flow at the CMB, secular core cooling, radiogenic heat production, latent heat associated to inner core crystallization, and gravitational energy due to chemical buoyancies, respectively (Labrosse, 2015; Landeau et al., 2022; Nimmo, 2007). It is well known that $\varnothing_{OC}$ is controlled by mantle properties; we discuss this matter in length below. Nevertheless, whatever are the sources of energy, there is a minimum heat flow $\varnothing_{OC}^{Min}$ that has to be extracted from the core to enable a TDD:

$$\varnothing_{OC}^{Min} = \varnothing_{Mag} + \varnothing_{OC}^{Cond} \quad (8)$$

with $\varnothing_{Mag}$ the heat flow that has to be extracted to compensate for the power dissipated to generate a dynamo from core convective motions and $\varnothing_{OC}^{Cond}$ the conductive heat flow along the temperature gradient, which we assume to be adiabatic (∇T_{Adiab}):

$$\varnothing_{OC}^{Cond} = k_{cond}.\nabla T_{Adiab} \quad (9)$$

In Eq. 9, we calculate ∇T_{Adiab} using the classical relation $\nabla T_{Adiab} = \alpha_{Fe}.g_0.T_{CMB}/C_p$, where α_{Fe}, g_0, T_{CMB} and Cp are thermal expansion, gravity, temperature and heat capacity of the outer core at the CMB, respectively.

Previous works proposed that $\varnothing_{Mag}$ originates from ohmic dissipation ($\varnothing_{Ohm}$) essentially (e.g. (Landeau et al., 2022; Nimmo, 2007)), which was estimated to roughly ~0.2 TW for the Earth (Christensen and Aubert, 2006; Stacey and Loper, 2007). In this work, we estimate $\varnothing_{Mag}$ calculating (Buffett, 2002):

$$\varnothing_{ohm} = \left(\frac{\eta_B B^2}{\mu_B l_B^2}\right) V_{Core} \quad (10)$$

where η_B, l_B, B and V_{core} are magnetic diffusivity, magnetic length, magnetic induction and the core volume, respectively. The l_B and B values may vary over time for the core of the planet under consideration. For simplicity, as proposed in (Buffett, 2002), we fixe l_B to 1.9 10^5 m and assume for B a current Earth-like value of 2.5 mT.

Then, we consider a Carnot-style efficiency for thermal convection to induce the magnetic field and obtain (Buffett, 2002; Monteux et al., 2011):

$$\varnothing_{Mag} = \varnothing_{Ohm} \Big/ \left(\frac{0.8\pi}{3} \frac{G\alpha_{Fe}\rho_{Fe}r_0^2}{C_p}\right) \quad (11)$$

where G, ρ_{Fe}, and r_0 are gravitational constant, average core density and outer core radius, respectively. This expression gives an estimation of the heat flow needed to compensate for the ohmic dissipation in the case of a thermally driven dynamo (i.e. we neglect the influence of the compositionally driven convection related to inner core solidification). For simplicity, we fix values of ρ_{Fe} to that of the Earth at 11420 kg/m^3. For the Earth, we find $\varnothing_{Mag}$=0.3 TW (all core parameters needed for these calculations are reported in Suppl. Table 3). We are aware that motions in the core may induce other energy contributions in Eq. 8 such as viscous dissipation. However, this term is likely small because kinetic energy is reported to be ~10^3 smaller than magnetic energy in the Earth's core (Gillet et al., 2010).

We now define the minimum secular cooling of a core compatible with sustaining a TDD, $\varnothing_{Cooling}^{Min}$, which is related to the minimum heat flow $\varnothing_{OC}^{Min}$. For this, we couple Eqs. (7) and (8):

$$\varnothing_{Cooling}^{Min} = \varnothing_{OC}^{Cond} + \varnothing_{Mag} - \varnothing_{Rad} - \varnothing_{Cryst} - \varnothing_{Buoy} \quad (12)$$

The different contributions to Eq. 12 have been detailed in several articles. Here, we consider $\varnothing_{Rad}$ arising from the radioactive disintegration of 50 ppm of potassium in the outer core (Bouhifd et al., 2007; Watanabe et al., 2014). Then, two different types of chemical buoyancy contributions should be considered:

(1) One arises from the release of light element upon crystallization of the inner core. For simplicity, we distribute it, as well as its associated $\varnothing_{Cryst}$ contribution, equally over the 4.5 *Ga* of the Earth history. Our reasons are (i) their minor overall contribution to $\varnothing_{Cooling}^{Min}$, compared to the other terms in Eq. 12 and (ii) we do not know the age of the inner core a priori.

(2) The chemical buoyancy term originating from CMB exsolutions of MgO and/or SiO_2 (Badro et al., 2016; Hirose et al., 2017; O'Rourke and Stevenson, 2016) is likely major just after the core formation. Its contribution should significantly decrease later on. This is because mixing between Fe-alloy and molten oxides is essentially restricted to the highest temperatures (>5000 K). A fast decay of the core temperature to ~4000 K on likely less than 1 million years after the Moon forming impact (Lebrun et al., 2013; Monteux et al., 2016) should result in ~1 wt% MgO (Badro et al., 2016) and 5–6 wt% SiO_2 (Hirose et al., 2017) in the Fe-alloy. This is not significantly different from the light elements content in the outer core today. Therefore, the contribution to the energy budget of chemical buoyancy term originating from CMB exsolutions is most likely minor over the last ~4 *Ga* of our planet's history.

4.3. Geodynamic modeling of the heat flow at the CMB

It is well established that the rate of core cooling is controlled by the ability of the overlaying mantle to evacuate heat and, as a consequence, by mantle properties. The heat flow at the CMB ($\varnothing_{LM}$; the mantle equivalent to $\varnothing_{OC}$) can be expressed using classical expressions developed for a convective mantle (Turcotte and Schubert, 2002):

$$\varnothing_{LM} = a_{Eff}\frac{k_m \Delta T}{L} Ra^{\beta} \; with \; Ra = \frac{\alpha_m g C p_m \rho_m^2 \Delta T L^3}{k_m \eta} \quad (13)$$

where ΔT and L are the CMB to surface temperature difference and distance, respectively. The signification of all the other parameters is provided in Suppl. Table 3. One could argue Eq. 13 remains approximate for faithful modeling of a convecting planetary mantle, because of its complexity and the number of parameters involved. Indeed, mantle dynamics may be specific to each terrestrial planet (see e.g. (Smrekar et al., 2018) for the case of Venus) and it may also evolve with the planet's age (as clearly happened to the Earth at the Archean to Proterozoic transition). Nevertheless, it remains that the terrestrial planets have common accretion mechanisms (Morbidelli et al., 2012) and probably all hosted a core-mantle segregation that yields to a hot core (Deguen et al., 2014). Therefore, we can expect that the global planetary parameters such as ΔT and L dominate the value of $\varnothing_{LM}$ in Eq. 13 to the first order, over other mantle complex features.

In Eq. 13, the values of a_{Eff} and β remain open to discussion. The β value depends on how the convective mantle is heated (basally or internally), but also on the value of the mantle Rayleigh number. For $Ra < 10^9$, (Wolstencroft et al., 2009) refined β to 0.29 or 0.33 for mantle convection induced by basal or internal heating, respectively. Interestingly, the value of 0.29 is very close to that of 2/7 proposed for a turbulent magma ocean with much larger Rayleigh number (Solomatov, 2000). Hence, we considered both β values in our models and, in each case, adjusted the value of a_{Eff} to fulfill the geodynamical constraints for the Earth. In particular, we use a_{Eff} (i) sufficiently high to produce $\varnothing_{LM} > \varnothing_{OC}^{Min}$, if thermal convection should play a role in maintaining the geomagnetic field and (ii) sufficiently low to be compatible with the energy budget of the core along the entire Earth's history (Fig. 7). In addition, we assume no significant change of the mantle dynamics in the planet history.

4.4. Powering a thermally driven dynamo in the Earth's outer core

We now calculate $\varnothing_{OC}^{Min}$ (Eq. 8), the minimum heat flow needed at the

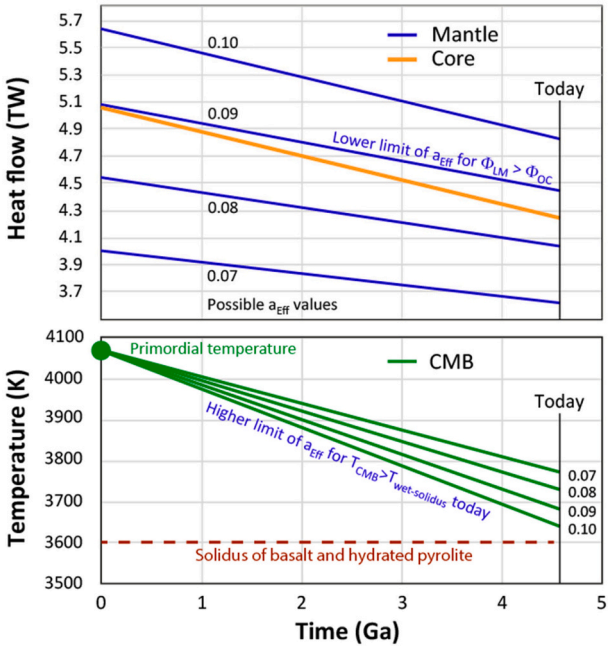

Fig. 7. Thermal state of the CMB along the Earth's history: (**A, top**) Outgoing heat flow at the CMB (Φ_{LM}, blue) is compatible with the power requirement to sustain a TDD ($\varnothing_{OC}^{Min}$, orange, Eq. 8) only for cooling efficiency of the mantle a_{Eff} higher than ~0.09 (Eq. 13, using $\beta = 0.29$, see text). (**B, bottom**) Cooling efficiency a_{Eff} higher than ~0.10 makes the current CMB temperature incompatible with melting of hydrated mantle materials (e.g. basalt, pyrolite) in the seismic ultra-low velocity zones. For $a_{Eff} = 0.09$, the CMB temperature decreases by ~380 K over ~4.5 billions of years. (For interpretation of the references to colour in this figure legend, the reader is referred to the web version of this article.)

CMB to power a purely terrestrial TDD. First, we need to set the initial thermal state at the CMB. A couple 100 thousand to a 1 million years after the Moon forming impact (MFI), solidification of the lowermost mantle reduced tremendously the heat flux at the CMB, compared to that prevailing in the global magma ocean period (Lebrun et al., 2013; Monteux et al., 2016). We consider an initial CMB temperature of 4065 K, which is ~200 K above the mantle solidus (Pierru et al., 2022). We note that such CMB temperature could also arise after a major meteoritic impact that would melt the lowermost mantle only partially.

Then, we calculate the heat flow $\varnothing_{OC}^{Min}$ (Eq. 8) in the outer core below the CMB as a function of time, including the contributions of (i) $\varnothing_{OC}^{Cond}$, the heat flux along the adiabatic gradient and (ii) ohmic dissipation necessary to power the geodynamo (typically ~0.2 TW for the Earth; (Christensen and Aubert, 2006; Stacey and Loper, 2007); see (Labrosse, 2015; Landeau et al., 2022); All parameters used here are reported in Suppl. Table 3). $\varnothing_{OC}^{Min}$ is the minimum heat flow at the CMB that can enable a TDD in the Earth's outer core. We calculate a primordial $\varnothing_{OC}^{Min}$ of 5.1 TW (Fig. 7a).

At this point, we need to consider that $\varnothing_{LM}$, the heat flow at the CMB is in fact controlled by mantle properties; $\varnothing_{LM}$ should be higher than $\varnothing_{OC}^{Min}$ to maintain an adiabatic gradient in the outer core and induce some thermal convection of the Fe-alloy, which can generate a magnetic field. $\varnothing_{LM}$ can be estimated using a classical approach of mantle dynamics (Turcotte and Schubert, 2002; Wolstencroft et al., 2009). Major parameters are the cooling efficiency of the mantle a_{Eff} and the exponential factor β (Eq. 13). With the selected set of parameters (Suppl. Table 3), considering $\varnothing_{LM} = \varnothing_{OC}^{Min}$ yields to a_{Eff} values of 0.09 or 0.05 for β values of 0.29 or 0.33, respectively. The β value of 0.29 is reportedly suited to model mantle convection induced by basal heating, which fits better our situation than $\beta = 0.33$ for internally heated mantle convection (Wolstencroft et al., 2009). a_{Eff} smaller than 0.09 (or 0.05 for $\beta = 0.33$) makes $\varnothing_{LM} < \varnothing_{OC}^{Min}$ and thus potentially a sub-adiabatic temperature gradient with no thermal convection in the outer core (Fig. 7a). If this value should represent the mantle cooling efficiency, then the geodynamo on Earth should be powered by other mechanisms, such as solutale convection and/or motions by astronomical forces (Andrault et al., 2016).

4.5. Thermal budget of the core over Earth's history

Yet secular cooling of the core occurs at a lower rate than the heat flow at the CMB, due to internal sources of energy (Eq. 12). Major ones are (i) radioactive disintegration of possibly 50 ppm of potassium in the outer core (Bouhifd et al., 2007; Watanabe et al., 2014) and (ii) latent heat and compositional energy of inner core crystallization. The former contribution decreases with time according to the ^{40}K half-life of ~1.25 billion years; the latter contribution operates only after formation of the inner core; other minor contributions may also exist. Since our goal is to model the cooling history of not only the Earth, but also other terrestrial planets with different thermochemical histories, we average all possible energy contributions by considering solely the full disintegration of ^{40}K present in 50 ppm of potassium, and distribute this energy evenly over a period of 4.5 billion years.

We perform this calculation for various value of a_{Eff}, the mantle cooling efficiency (Fig. 7). A first observations is that a_{Eff} values of 0.09 to 0.1 (for $\beta = 0.29$) are nicely compatible with the classical view of the core thermal history. It yields an integrated amplitude of core cooling (ΔT) of 380 to 450 K over the 4.5 billion years of the Earth's history (Fig. 7b). If the primordial CMB temperature was 4065 K, which is ~200 K above the solidus of the pyrolitic-mantle (Pierru et al., 2022), the temperature is ~3650(150) K today. This is slightly above the solidus temperatures of mid-ocean ridge basalt (Andrault et al., 2014) and water-bearing pyrolite (Nomura et al., 2011), which were both reported at ~3600 K. Accordingly, the seismic ultra-low velocity zones atop the CMB can be explained by melting of these materials. The rate of core cooling is compatible with the onset of inner core crystallization 1.9(4) billion years ago. It is the time needed to cool the core by 150 K, which corresponds to the growth of the inner core up to its present-day radius (Anzellini et al., 2013).

Interestingly, we find that both $\varnothing_{LM}$ and $\varnothing_{OC}^{Min}$, which we recalculate at each time step, decrease similarly with secular cooling of the CMB (Fig. 7b). The parallelism found between these evolutions shows that once conditions are reached to enable a thermally driven magnetic field (i.e. $\varnothing_{LM} > \varnothing_{OC}^{Min}$), the geodynamo should be maintained until the outer core is solidified. It also shows that $\varnothing_{LM} > \varnothing_{OC}^{Min}$ can be achieved for a large range of primordial thermal state of the planet interior. In particular, Moon-forming impacts may not be required for long-lived magnetic field. For further application to other terrestrial planets, we consider that $a_{Eff} \sim 0.09$ and $\beta = 0.29$ could represent well the cooling efficiency of Earth-like planetary mantle. We note that parallel calculations with $a_{Eff} \sim 0.05$ and $\beta = 0.33$ provide very similar conclusions.

4.6. Conditions for powering a dynamo on Earth like planets

As TDDs can be established when $\varnothing_{LM} > \varnothing_{OC}^{Min}$, we can estimate the likelihood of dynamos on Earth-like terrestrial planets of different radii and relative core sizes. We do not consider the latent heat and compositional energy of possible inner core crystallization, therefore restricting our analyses to pure TDD. As for the Earth, we evaluate the heat flow in the outer core from the γ-k_{Cond} model for the Fe-alloy (Eqs. (2), (4) and (6) and Table 2) and that in the mantle from Eq. 13. This assumes that a planet's mantle has a similar efficiency to Earth in cooling its core (see Methods). We also assume the primordial CMB temperature to be that of the solidus of a pyrolitic mantle solidus at the CMB pressure. All density calculations assume that the composition of the planetary mantle and

core is the same as that of the Earth.

Calculations show that the relative size of the planetary core (V_{Core}/V_{Planet}) is critical to define the planet parameters compatible, or not, with the powering of a TDD (Fig. 8a). The results present a maximum V_{Core}/V_{Planet} ratio of 25 vol% for planets with a volume of ~1.2 times that of the Earth. The origin of this maximum is the change of slope at ~160 GPa in the evolution of k_{Cond} with the P-T conditions of planetary CMBs (Fig. 6). The maximum relative core size compatible with powering a TDD decreases relatively fast for planet volumes away from this maximum. The critical V_{Core}/V_{Planet} ratio is found ~15 % and 10 % for planets twice smaller or 50 % larger than the Earth, respectively. Before further analyses, we recall that the limits drawn between fields favorable or not to production of a TDD (Fig. 8a, as well as or Fig. 8b, see below) do not predict the possible powering of a magnetic field by other energy sources, such as chemical buoyancy or mechanical forcing by astronomical forces (i.e. precession and tides; e.g. (Malkus, 1968)). In addition, the position of the lines may change slightly, if the planetary dynamics is significantly different of that of the Earth, making unfit the use of parameters $a_{Eff} = 0.09$ and $\beta = 0.29$ in Eq. 13.

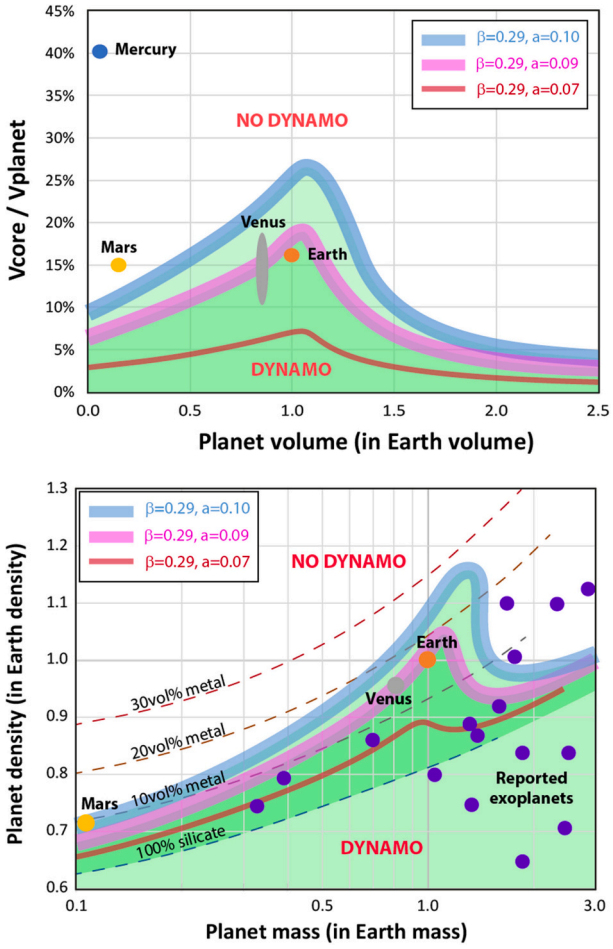

Fig. 8. Critical planetary parameters for thermally driven dynamo (TDD). Planets below blue lines have heat flow at the basis of their mantle larger than in the outer core ($\varnothing_{LM} > \varnothing_{OC}^{Min}$), which is critically required to develop convection in the outer core and a TDD. **(A, top) Planets of the solar system.** A mantle cooling efficiency $a_{Eff} = 0.09$ and $\beta = 0.29$ (see Eq. 13) is compatible with the presence of a TDD on Earth and absence of dynamo on Mars and Venus, if the core of Venus core is large (as proposed by (Dumoulin et al., 2017)). Same results are obtain for $\beta = 0.33$ (see text). **(B, Bottom) Exoplanets**: The reported exoplanets (blue dots) lighter than 1.5 Earth mass could be hosting a TDD, if their mantles have similar efficiency than that of the Earth to generate a steady heat flow at the CMB (e.g. $a_{Eff} = 0.09$). For heavier exoplanets, the less dense may be hosting a TDD, if they truly host a core of significant size. In both upper and lower frames, the maxima found at planet volume/mass just above that of the Earth is generated by the change of slope in k_{Cond} at ~160 GPa (Fig. 6). (For interpretation of the references to colour in this figure legend, the reader is referred to the web version of this article.)

With a V_{Core}/V_{Planet} ratio of ~40 %, Mercury plots far above the field of core size compatible with a TDD. Still, Mercury hosts a magnetic field of low intensity, which remains an intense subject of debates. It has been proposed that the long-lived dynamo action could be maintained by the latent heat of crystallization of a core possibly composed of a Fe—Si alloy (Davies et al., 2024; Knibbe and van Westrenen, 2018).

The characteristics of Mars' core plot much closer, but still outside the field favorable to TDD. It is compatible with the absence of an active magnetic field. Still, it is well accepted that Mars hosted a magnetic field earlier in its history. As proposed for Mercury, the driving force could be chemical buoyancy: (i) CMB exsolutions resulting from core-mantle disequilibrium after the core formation processes, and/or (ii) solidification of its core likely composed of a Fe—S alloy.

The situation remains open for Venus because its inner structure is barely constrained, especially the relative core size (Dumoulin et al., 2017). A core larger than ~15 % of the planet volume would drive Venus outside of the field where $\varnothing_{LM} > \varnothing_{OC}^{Min}$, thus disabling a TDD (Fig. 8a). This would be compatible with a present-day absence of a magnetic field. For Venus, we do not know if a dynamo was active earlier in the planet history. We note that Venus would definitely plot outside the field favorable to TDD, whatever its core size, if the value of a_{Eff} would be 0.08 or 0.07 (Fig. 8). In such case the Earth as well would plot outside the field and, to explain the geodynamo, one should consider either mechanical forcing by astronomical forces (see (Andrault et al., 2016; Malkus, 1968)) and/or chemical buoyancy, noting that this last term cannot apply to (inner-core free) Archean geodynamo (Tarduno et al., 2015). For $a_{Eff} \sim 0.07$, CMB cooling over the Earth history would $\Delta T = 300$ K (Fig. 7).

A final implication concerns exoplanets. We calculate the critical planet density for enabling a TDD, assuming mantle and core densities similar to that of the Earth. The lower the exoplanet's density, the smaller its core is likely to be and, according to Fig. 8a, the easier a TDD. When reporting our constraints on dynamo viability into the relevant planet-mass vs planet-density diagram (Luque and Pallé, 2022), most of the Earth-like exoplanets reported today fall within the field favorable to occurrence of a TDD (Fig. 8b). Still, the exoplanets 1.5 times heavier than the Earth and with similar to larger densities fall outside. This conclusion is not much affected by our assumptions: (i) the result is similar considering a_{Eff} values between 0.07 and 0.10; (ii) Considering a saturation limit for Fe-alloy resistivity of 2500 K instead of 3000 K (see Methods) would make k_{Cond} higher and the $\varnothing_{OC}^{Min}$ requirement higher. Finally, one can wonder if exoplanets with average density lower than that expected for a full silicate mantle (i.e. line noted "100 % silicate" in Fig. 8b) contain a significant metallic core. Altogether, an exoplanet presenting the highest chances to host a TDD has a mass up to 1.5 that of the Earth, and a relative core volume up to 10 % or 15 %, for a mass smaller or larger, than ~80 % that of the Earth, respectively.

Credit authorship contribution statement

D. Andrault: Writing – review & editing, Writing – original draft, Visualization, Validation, Supervision, Resources, Project administration, Methodology, Investigation, Funding acquisition, Conceptualization. **L. Pison Pacynski:** Visualization, Validation, Methodology, Investigation, Formal analysis, Data curation. **J. Monteux:** Writing – review & editing, Writing – original draft, Visualization, Validation, Supervision, Software, Methodology, Formal analysis, Data curation. **E. Gardés:** Writing – original draft, Visualization, Validation, Supervision, Resources, Methodology, Investigation, Formal analysis, Data curation. **A. Mathieu:** Validation, Resources, Methodology, Conceptualization.

Declaration of competing interest

The authors declare that they have no known competing financial interests or personal relationships that could have appeared to influence the work reported in this paper.

Data availability

Data are reported in the main article and supplementary information files

Acknowledgements

We thank D. Cébron, N. Jaisle, and G. Morard for fruitful discussions on the LH-DAC experiments and modeling, and useful comments from Chris Davis and an anonymous reviewer. This work has been supported by the *Programme National de Planetologie* (PNP-INSU-CNRS) and the *ClerVolc Program of Excellence* (contribution n°679).

Appendix A. Supplementary data

Supplementary data to this article can be found online at https://doi.org/10.1016/j.pepi.2025.107315.

References

Anderson, O.L., 1998. The Grüneisen parameter for iron at outer core conditions and the resulting conductive heat and power in the core. Phys. Earth Planet. Inter. 109, 179–197.
Andrault, D., 2019. Thermodynamical constraints on the crystallization of a deep magma-ocean on earth. C. R. Geosci. 351, 221–228.
Andrault, D., Pesce, G., Bouhifd, M.A., Bolfan-Casanova, N., Henot, J.M., Mezouar, M., 2014. Melting of subducted basalt at the core-mantle boundary. Science 344, 892–895.
Andrault, D., Monteux, J., Le Bars, M., Samuel, H., 2016. The deep earth may not be cooling down. Earth Planet. Sci. Lett. 443, 195–203.
Anzellini, S., Dewaele, A., Mezouar, M., Loubeyre, P., Morard, G., 2013. Melting of Iron at Earth's inner Core boundary based on fast X-ray diffraction. Science 340, 464–466.
Badro, J., Siebert, J., Nimmo, F., 2016. An early geodynamo driven by exsolution of mantle components from Earth's core (vol 536, pg 326, 2016). Nature 539, 326–328.
Berrada, M., Secco, R.A., 2021. Review of electrical resistivity measurements and calculations of Fe and Fe-alloys relating to planetary cores. Front. Earth Sci. 9.
Bouhifd, M.A., Gautron, L., Bolfan-Casanova, N., Malavergne, V., Hammouda, T., Andrault, D., Jephcoat, A.P., 2007. Potassium partitioning into molten iron alloys at high-pressure: implications for Earth's core. Phys. Earth Planet. Inter. 160, 22–33.
Buffett, B.A., 2002. Estimates of heat flow in the deep mantle based on the power requirements for the geodynamo. Geophys. Res. Lett. 29.
Buffett, B.A., 2014. Geomagnetic fluctuations reveal stable stratification at the top of the Earth's core. Nature 507, 484–487.
Bulatov, K.M., Semenov, A.N., Bykov, A.A., Machikhin, A.S., Litasov, K.D., Zinin, P.V., Rashchenko, S.V., 2020. Measurement of thermal conductivity in laser-heated diamond anvil cell using radial temperature distribution. High Pressure Res. 40, 315–324.
Christensen, U.R., Aubert, J., 2006. Scaling properties of convection-driven dynamos in rotating spherical shells and application to planetary magnetic fields. Geophys. J. Int. 166, 97–114.
Davies, C., Pozzo, M., Gubbins, D., Alfe, D., 2015. Constraints from material properties on the dynamics and evolution of Earth's core. Nat. Geosci. 8, 678.
Davies, C.J., Pommier, A., Greenwood, S., Wilson, A., 2024. Thermal and magnetic evolution of mercury with a layered Fe-Si(-S) core. Earth Planet. Sci. Lett. 641, 118812.
Deguen, R., Landeau, M., Olson, P., 2014. Turbulent metal-silicate mixing, fragmentation, and equilibration in magma oceans. Earth Planet. Sci. Lett. 391, 274–287.
Dumoulin, C., Tobie, G., Verhoeven, O., Rosenblatt, P., Rambaux, N., 2017. Tidal constraints on the interior of Venus. J. Geophys. Res. 122, 1338–1352.
Farah, F., Lee, K.K.M., Akin, M.C., 2022. Temperature distribution in a laser-heated diamond anvil cell as described by finite element analysis. AIP Adv. 12, 105218.
Garai, J., Chen, J., Telekes, G., 2011. PVT equation of state of epsilon iron and its densities at inner core conditions. Am. Miner. 96, 828–832.
Gillet, N., Jault, D., Canet, E., Fournier, A., 2010. Fast torsional waves and strong magnetic field within the Earth's core. Nature 465, 74–77.
Gomi, H., Yoshino, T., 2018. Impurity resistivity of fcc and hcp Fe-based alloys: thermal stratification at the top of the Core of super-earths. Front. Earth Sci. 6.
Gomi, H., Ohta, K., Hirose, K., Labrosse, S., Caracas, R., Verstraete, M.J., Hernlund, J.W., 2013. The high conductivity of iron and thermal evolution of the Earth's core. Phys. Earth Planet. Inter. 224, 88–103.
Hemley, R.J., Mao, H.-K., Shen, G., Badro, J., Gillet, P., Hanfland, M., Häusermann, D., 1997. X-ray imaging of stress and strain of diamond, Iron, and tungsten at Megabar pressures. Science 276, 1242–1245.
Hirose, K., Morard, G., Sinmyo, R., Umemoto, K., Hernlund, J., Helffrich, G., Labrosse, S., 2017. Crystallization of silicon dioxide and compositional evolution of the Earth's core. Nature 543, 99-+.
Hsieh, W.-P., Goncharov, A.F., Labrosse, S., Holtgrewe, N., Lobanov, S.S., Chuvashova, I., Deschamps, F., Lin, J.-F., 2020. Low thermal conductivity of iron-silicon alloys at Earth's core conditions with implications for the geodynamo. Nat. Commun. 11, 3332.
Knibbe, J.S., van Westrenen, W., 2018. The thermal evolution of Mercury's Fe–Si core. Earth Planet. Sci. Lett. 482, 147–159.
de Koker, N., Steinle-Neumann, G., Vlček, V., 2012. Electrical resistivity and thermal conductivity of liquid Fe alloys at high P and T, and heat flux in Earth's core. Proc. Natl. Acad. Sci. U. S. A. 109, 4070–4073.
Konôpková, Z., Lazor, P., Goncharov, A.F., Struzhkin, V.V., 2011. Thermal conductivity of hcp iron at high pressure and temperature. High Pressure Res. 31, 228–236.
Konôpková, Z., McWilliams, R.S., Gómez-Pérez, N., Goncharov, A.F., 2016. Direct measurement of thermal conductivity in solid iron at planetary core conditions. Nature 534, 99.
Labrosse, S., 2015. Thermal evolution of the core with a high thermal conductivity. Phys. Earth Planet. Inter. 247, 36–55.
Landeau, M., Fournier, A., Nataf, H.-C., Cébron, D., Schaeffer, N., 2022. Sustaining Earth's magnetic dynamo. Nat. Rev. Earth Environ. 3, 255–269.
Lebrun, T., Massol, H., Chassefiere, E., Davaille, A., Marcq, E., Sarda, P., Leblanc, F., Brandeis, G., 2013. Thermal evolution of an early magma ocean in interaction with the atmosphere. J. Geophys. Res. 118, 1155–1176.
Lobanov, S.S., Geballe, Z.M., 2022. Non-isotropic contraction and expansion of samples in diamond anvil cells: implications for thermal conductivity at the Core-mantle boundary. Geophys. Res. Lett. 49, e2022GL100379.
Luque, R., Pallé, E., 2022. Density, not radius, separates rocky and water-rich small planets orbiting M dwarf stars. Science 377, 1211–1214.
Malkus, W.V.R., 1968. Precession of the earth as the cause of geomagnetism. Science 160, 259–264.
Manthilake, G., Chantel, J., Monteux, J., Andrault, D., Bouhifd, M.A., Bolfan-Casanova, N., Boulard, E., Guignot, N., King, A., Itie, J.P., 2019. Thermal conductivity of FeS and its implications for Mercury's long-sustaining magnetic field. J. Geophys. Res. 124, 2359–2368.
McNamara, A.K., Garnero, E.J., Rost, S., 2010. Tracking deep mantle reservoirs with ultra-low velocity zones. Earth Planet. Sci. Lett. 299, 1–9.
McWilliams, R.S., Konôpková, Z., Goncharov, A.F., 2015. A flash heating method for measuring thermal conductivity at high pressure and temperature: application to Pt. Phys. Earth Planet. Inter. 247, 17–26.
Metzner, D., Olbrich, M., Lickschat, P., Horn, A., Weißmantel, S., 2020. Experimental and theoretical determination of the effective penetration depth of ultrafast laser radiation in stainless steel. Lasers Manufact. Mater. Process. 7, 478–495.
Miller, G.H., Stolper, E.M., Ahrens, T.J., 1991. The equation of state of a molten komatiite 2. Application to komatiite Petrogenesis and the hadean mantle. J. Geophys. Res. 96, 11849–811864.
Monteux, J., Jellinek, A.M., Johnson, C.L., 2011. Why might planets and moons have early dynamos? Earth Planet Sci. Lett. 310, 349–359.
Monteux, J., Andrault, D., Samuel, H., 2016. On the cooling of a deep terrestrial magma ocean. Earth Planet. Sci. Lett. 448, 140–149.
Morard, G., Andrault, D., Antonangeli, D., Bouchet, J., 2014. Properties of iron alloys under the Earth's core conditions. C. R. Geosci. 346, 130–139.
Morbidelli, A., Lunine, J.I., O'Brien, D.P., Raymond, S.N., Walsh, K.J., 2012. Building terrestrial planets. In: Jeanloz, R. (Ed.), Annual Review of Earth and Planetary Sciences, 40, pp. 251–275.
Nakajima, M., Stevenson, D.J., 2015. Melting and mixing states of the Earth's mantle after the moon-forming impact. Earth Planet. Sci. Lett. 427, 286–295.
Nimmo, F., 2007. Energetics of the Core, pp. 31–65.
Nishi, T., Shibata, H., Waseda, Y., Ohta, H., 2003. Thermal conductivities of molten iron, cobalt, and nickel by laser flash method. Metall. Mater. Trans. A 34, 2801–2807.
Nomura, R., Ozawa, H., Tateno, S., Hirose, K., Hernlund, J.W., Muto, S., Ishii, H., Hiraoka, N., 2011. Spin crossover and iron-rich silicate melt in the Earth's deep mantle. Nature 473, 199–202.
Ohta, K., Nishihara, Y., Sato, Y., Hirose, K., Yagi, T., Kawaguchi, S.I., Hirao, N., Ohishi, Y., 2018. An experimental examination of thermal conductivity anisotropy in hcp Iron. Front. Earth Sci. 6.
O'Rourke, J.G., Stevenson, D.J., 2016. Powering Earth's dynamo with magnesium precipitation from the core. Nature 529, 387.
Pierru, R., Pison, L., Mathieu, A., Gardés, E., Garbarino, G., Mezouar, M., Hennet, L., Andrault, D., 2022. Solidus melting of pyrolite and bridgmanite: implication for the thermochemical state of the Earth's interior. Earth Planet. Sci. Lett. 595, 117770.
Pourovskii, L.V., Mravlje, J., Pozzo, M., Alfè, D., 2020. Electronic correlations and transport in iron at Earth's core conditions. Nat. Commun. 11, 4105.
Pozzo, M., Davies, C., Gubbins, D., Alfè, D., 2012. Thermal and electrical conductivity of iron at Earth's core conditions. Nature 485, 355–399.
Pozzo, M., Davies, C.J., Alfè, D., 2022. Towards reconciling experimental and computational determinations of Earth's core thermal conductivity. Earth Planet. Sci. Lett. 584, 117466.
Qaddah, B., Monteux, J., Le Bars, M., 2020. Thermal evolution of a metal drop falling in a less dense, more viscous fluid. Phys. Rev. Fluids 5.
Saha, P., Mazumder, A., Mukherjee, G.D., 2020. Thermal conductivity of dense hcp iron: direct measurements using laser heated diamond anvil cell. Geosci. Front. 11, 1755–1761.

Secco, R.A., 2017. Thermal conductivity and Seebeck coefficient of Fe and Fe-Si alloys: implications for variable Lorenz number. Phys. Earth Planet. Inter. 265, 23–34.
Silber, R.E., Secco, R.A., Yong, W.J., Littleton, J.A.H., 2019. Heat flow in Earth's Core from invariant electrical resistivity of Fe-Si on the melting boundary to 9 GPa: do light elements matter? J. Geophys. Res. 124, 5521–5543.
Smrekar, S.E., Davaille, A., Sotin, C., 2018. Venus Interior structure and dynamics. Space Sci. Rev. 214, 88.
Solomatov, V.S., 2000. Fluid dynamics of terrestrial magma ocean. In: Canup, R.M., Righter, K. (Eds.), Origin of the Earth and Moon. The University of Arizona Press, Tucson, Arizona, pp. 323–338.
Stacey, F.D., Loper, D.E., 2007. A revised estimate of the conductivity of iron alloy at high pressure and implications for the core energy balance. Phys. Earth Planet. Inter. 161, 13–18.
Stixrude, L., de Koker, N., Sun, N., Mookherjee, M., Karki, B.B., 2009. Thermodynamics of silicate liquids in the deep earth. Earth Planet. Sci. Lett. 278, 226–232.
Tarduno, J.A., Cottrell, R.D., Davis, W.J., Nimmo, F., Bono, R.K., 2015. A hadean to Paleoarchean geodynamo recorded by single zircon crystals. Science 349, 521–524.
Turcotte, D.L., Schubert, G., 2002. Geodynamics, 2 ed. Cambridge University Press, Cambridge.
Wagle, F., Steinle-Neumann, G., de Koker, N., 2019. Resistivity saturation in liquid iron-light-element alloys at conditions of planetary cores from first principles computations. C. R. Geosci. 351, 154–162.
Watanabe, K., Ohtani, E., Kamada, S., Sakamaki, T., Miyahara, M., Ito, Y., 2014. The abundance of potassium in the Earth's core. Phys. Earth Planet. Inter. 237, 65–72.
Williams, Q., 2018. The thermal conductivity of Earth's core: A key geophysical parameter's constraints and uncertainties. In: Jeanloz, R., Freeman, K.H. (Eds.), Annu. Rev. Earth Planet. Sci, pp. 47–66.
Wolstencroft, M., Davies, J.H., Davies, D.R., 2009. Nusselt–Rayleigh number scaling for spherical shell Earth mantle simulation up to a Rayleigh number of 109. Phys. Earth Planet. Inter. 176, 132–141.
Xu, J., Zhang, P., Haule, K., Minar, J., Wimmer, S., Ebert, H., Cohen, R.E., 2018. Thermal conductivity and electrical resistivity of solid Iron at Earth's Core conditions from first principles. Phys. Rev. Lett. 121, 096601.
Yong, W., Secco, R.A., Littleton, J.A.H., Silber, R.E., 2019. The Iron invariance: implications for thermal convection in Earth's Core. Geophys. Res. Lett. 46, 11065–11070.